A Single-Stage Bi-directional AC-DC Converter with no Electrolytic Capacitor for EV

Behnam Koushki, Praveen Jain, Alireza Bakhshai
Department of Electrical and Computer Engineering
Queen's University
Kingston ON, Canada
11fbk@queensu.ca

***Abstract*— An isolated, single-stage bi-directional AC-DC converter for electric vehicle battery charger with no electrolytic capacitor and 8 active switches is proposed. The proposed converter prevents low frequency power ripple from going to the battery. This prevents extra heat production in the battery and consequently causes the battery to last longer. No use of an electrolytic capacitor in the circuit increases the reliability of the system. To control the circuit, a four- part controller is proposed. The controller obtains ZVS for all the active switches while it optimizes the performance of the system in terms of conduction losses. Simulation results with PSIM, and experimental results to verify the theory, have been carried out.**

Keywords—resonant converter; Dual Active Bridge converter; ZVS; EV charge; Electrolytic Capacitor less; Bi-directional AC-DC converter; V2G; power decoupling circuit;

I. INTRODUCTION

Electric Vehicles (EV's) are becoming more popular due to their zero fuel usage, and zero emission. [1]. Bidirectional power flow through the charger enables the grid to utilize the battery of the mass of the cars, parked in the parking yards, as its energy storage [2]. On-board bi-directional battery chargers for medium power (1-3Kw) have been extensively researched recently [3,4,5]. Single-stage or two-stage topologies can be used for battery charger [6]. In general, single-stage topologies such as [2, 3 and 4] are known for lower power component count and compactness. Most of the topologies, including single-stage and two-stage topologies, use an electrolytic capacitor to absorb the 120/100Hz power produced through the single-stage AC-DC power conversion. Electrolytic capacitor, or in short E-cap, has a limited lifetime and reduces the reliability of the system. Some topologies let the 100/120Hz power go to the battery [7]. This low frequency power ripple produces extra heat inside the battery, which results in reduction of the lifespan of the battery [8].

Different single-stage and two stage topologies with no E-cap have been presented recently [9-11]. Though they are reliable to due no use of E-cap, they all pass the low frequency power to the battery, which is not favorable. In [12] a single-stage topology with no E-cap utilizing a single-stage AC-DC HB-FB resonant converter plus a separate decoupling circuit on the DC-side were presented as a bi-directional EV charger. Active filter absorbs the low frequency power and the battery current is DC.

In this paper, the AC-DC HB-FB topology with an active filter integrated to the FB side to absorb the 120Hz power is proposed. The topology has one less leg compared to [12]. In addition, unlike [12], there is a possibility that resonant current helps to obtain ZVS for the shared leg. This room can be used to improve the performance of the converter. Since one leg is shared between two circuits, the control is completely different form [12].To enable the topology to work with a different range of power and power angle, a four-part controller is proposed. The controller minimizes the conduction losses, obtains ZVS for all the switches, and transfers the power bi-directionally while no low frequency current ripple penetrates to the battery. ZVS enables the switching frequency to increase. Higher switching frequency enables use of smaller reactive components.

In continue, first the topology is described, and then the analysis is given. Following that, the controller is described. The design and calculation results will come afterwards and finally the simulation and experimental results are presented.

II. TOPOLOGY AND ANALISYS

The proposed topology is shown in Fig.1. It consists of an LC grid-side filter, a dual active bridge (HB-FB) series resonant AC-DC converter, an integrated buck-type active filter on the DC-side, and a LC battery-side filter.

A. Decoupling Circuit

Let's assume that d_1, d_2, and d_3 are the duty-cycles of the upper switches of the legs I, II, and III respectively; φ_{12} is the phase-shift between leg I and II and φ_{23} is the phase-shift between leg II and III. If v_g is the grid voltage, P_m is the peak power, θ_g is the grid current angle and ω_g is the angular grid frequency, the AC and DC parts of power are shown in (1) and (2) respectively. The converter transfers instantaneous power p_t shown in (4) from the grid.

$$p_{ac} = P_m \cos(2\omega_g t + \theta_g) \quad (1)$$

$$p_{dc} = P_m \cos(\theta_g) \quad (2)$$

$$p_t = p_{ac} + p_{dc} \quad (3)$$

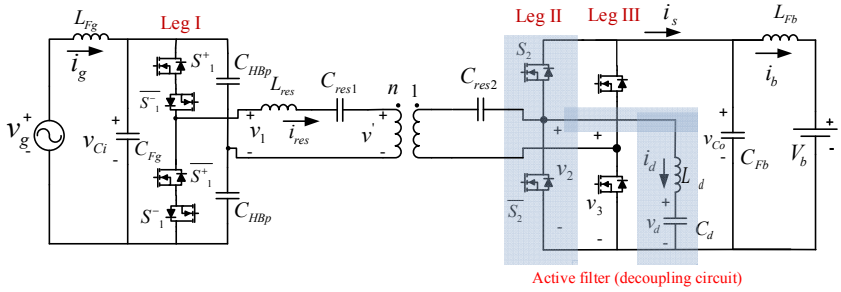

Fig. 1. Proposed topology.

d_2 is controlled in such a way that all of the AC power goes to the decoupling capacitor C_d. Provided that all the AC power shown in (1) is absorbed by the decoupling capacitor, v_d is shown in (4).

$$v_d = \sqrt{{V_0}^2 + (P_m/C_d\omega_g)(\sin(2\omega_g t + \theta) - \sin(\theta))} \quad (4)$$

The decoupling circuit controller make v_d follow the reference shown in (4)(4). Decoupling inductor current i_d is shown in Fig.2(a) with green color. The peak and valley values of this inductor can be calculated from the buck converter equations in CCM mode and they are shown in (5) and (6) **Error! Reference source not found.**respectively.

$$i_{dp} = i_{dav} + \frac{d_2}{L_d f_s}(v_{Co} - v_d) \quad (5)$$

$$i_{dv} = i_{dav} - \frac{d_2}{L_d f_s}(v_{Co} - v_d) \quad (6)$$

L_d is the decoupling circuit inductor and f_s is the switching frequency.

B. Resonant Circuit

To control the power transferred, p_t, duty cycles d_1 and d_3 and phase-shifts φ_{12} and φ_{23} are used. In addition to transfer the power, ZVS should be achieved for all the switches shown in Fig.2(a). To obtain the ZVS conditions for the switching instants $t_0 - t_5$ as well as power transfer equations, resonant circuit which is the heart of the topology is considered. Switching actions of leg I, II and III applies pulse voltages v_1, v_2 and v_3 across the resonant circuit. For the ease of calculation, all these pulse voltages are transferred to the primary side of the transformer and are shown in Fig.2(a).To analyze the resonant circuit, a phasor model is used as shown in Fig.2(b). For every variable y in the resonant circuit, $\bar{Y} = |\bar{Y}|e^{j\measuredangle Y}$ shows its related phasor at the switching frequency f_s. defining function f shown in (7) helps with calculations. The magnitude of $\bar{V}_1$ can be written using this function as is shown in (8).

$$f(d_i) = \frac{2}{\pi}\sqrt{2(1-\cos(2\pi d_i))}, i = 1.2.3. \quad (7)$$

$$|\bar{V}_1| = f(d_1)|v_{Ci}|, \quad (8)$$

The power transferred through the resonant tank can be shown in (9). In this equation, X is the reactance of the resonant branch at the switching frequency and is shown in (9).

$$p_t = \frac{1}{X} f(d_1)|v_{Ci}||\overline{I_{res}}|\cos(-\pi d_1 - \measuredangle\overline{I_{res}}) \quad (9)$$

$$X = L_{res}\omega - 1/(C_{res}\omega) \quad (10)$$

$$\omega = 2\pi f_s \quad (11)$$

For a given p_t and d_1, $\measuredangle\overline{I_{res}}$ can be found from (9). Then writing the KVL in the only loop in the circuit shown in Fig.2(b) yields the $|\overline{V'_s}|$ as is shown in (12).

$$|\overline{V'_s}| = \sqrt{(X|\overline{I_{res}}|)^2 + |\bar{V}_1|^2 - 2X\sqrt{(|\bar{V}_1||\overline{I_{res}}|)^2 - p_t^2}} \quad (12)$$

For every d_2 and $|\overline{V'_s}|$, the φ_{23} that synthesizes $\bar{V}_s$ with the magnitude of $|\overline{V'_s}|$, is shown in (13).

$$\varphi_{23} = \left(\frac{1}{2\pi}\right)\text{acos}\left(\frac{-|\overline{V'_s}|^2 + |\overline{V_2}|^2 + |\overline{V_3}|^2}{2|\overline{V_2}||\overline{V_3}|}\right) + 0.5(d_2 - d_3) \quad (13)$$

One more important equation to derive is the equation of φ_{12}. To find this equation, first M, the angle of $\overline{V'_s}$ when origin in Fig.2(a) is shifted from zero to t_2, is derived and shown in (14). From this equation, and the angle of $\overline{V'_s}$ which can be calculated form the KVL in the loop in Fig.2(b), φ_{12} can be obtained and is shown in (15).

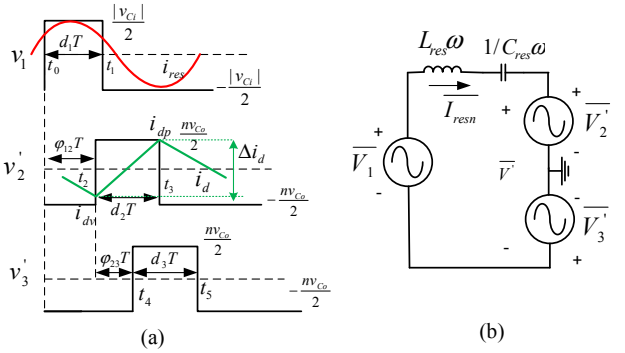

Fig. 2. Pulse voltages applied to the resonant circuit.(b) Resonant circuit in phasor domain.

$$M = \tan^{-1}\frac{(-\mathrm{f}(d_2)\sin\pi d_2 + \mathrm{f}(d_3)\sin(\pi d_3 + 2\pi\varphi_{23}))}{(\mathrm{f}(d_2)\cos\pi d_2 - \mathrm{f}(d_3)\cos(\pi d_3 + 2\pi\varphi_{23}))} \quad (14)$$

$$\varphi_{12} = \frac{1}{2\pi}(M - 2\pi d_1 - \measuredangle\overline{V_s'}) \quad (15)$$

The necessary ZVS conditions for the switching instants t_0 to t_5 can be calculated from the phasor model. For legs I and II which are not shared they are shown in (16)-(19)

$$|\overline{I_{res}}|\cos(\measuredangle\overline{I_{res}}) < -\varepsilon_1 \quad (16)$$

$$|\overline{I_{res}}|\cos(2\pi d_1 + \measuredangle\overline{I_{res}}) > \varepsilon_1 \quad (17)$$

$$|\overline{I_{res}}|\cos(2\pi(\varphi_{12} + (\varphi_{23}) + \measuredangle\overline{I_{res}}) < -\varepsilon_2 \quad (18)$$

$$|\overline{I_{res}}|\cos(2\pi d_3 + 2\pi(\varphi_{12} + (\varphi_{23}) + \measuredangle\overline{I_{res}}) > \varepsilon_2 \quad (19)$$

For the leg II with switching instants t_2 and t_3, the ZVS conditions does not only depend on the resonant current as decoupling inductor current, i_d is also coming out from the midpoint of this led. The ZVS conditions for this leg is shown in (20) and (21) in which i_{dp} and i_{dv} are the peak value and valley value of the i_d as shown in Fig.2(a).

$$-|\overline{I_{res}}|\cos(2\pi\varphi_{12} + \measuredangle\overline{I_{res}}) + i_{dp} < -\varepsilon_2 \quad (20)$$

$$-|\overline{I_{res}}|\cos(2\pi\varphi_{12} + 2\pi d_2 + \measuredangle\overline{I_{res}}) + i_{dv} > \varepsilon_2 \quad (21)$$

ε_1 and ε_2 are minimum current needed to charge and discharge the snubber capacitors C_s across each switch within a desired dead time t_q and they are shown in (22) and (23).

$$\varepsilon_1 = C_s\frac{|v_{Ci}|}{t_q} \quad (22)$$

$$\varepsilon_2 = C_s\frac{v_{Co}}{t_q} \quad (23)$$

These equations are used in the resonant controller, which is responsible for obtaining ZVS for all of the switching instants.

III. CONTROLLER

Fig.3(a) shows the block diagram of the controller. It has four major parts: grid controller, decoupling circuit controller, resonant circuit controller, and supervisory controller. Since the operation of active filter controller and supervisory controller is similar to our previous work [12-13] and enough discussion about them was given there, here more attention is paid to the grid controller. In addition, resonant controller, which is very different, is described here.

A. Grid Cotroller

The grid controller can be either a proportional resonant (PR) controller or PI controllers in d-q coordinates. Fig.3(b) shows a

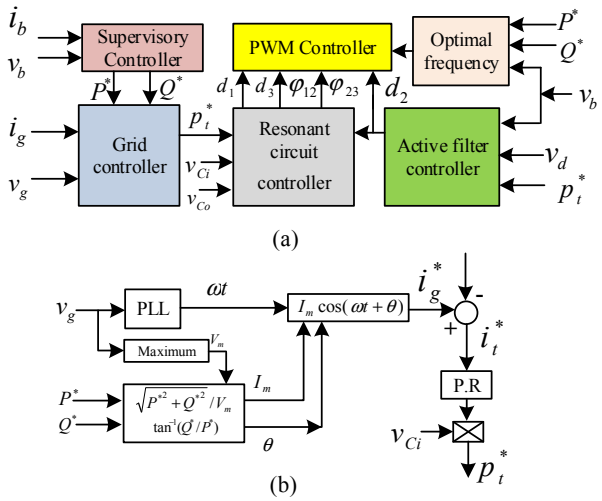

Fig. 3. Proposed controller: (a) its building blocks and (b) grid controller with P.R controller.

P.R grid controller. From the references for active and reactive power, P^* and Q^*, sent from the supervisory controller, the grid controller first calculates the magnitude, I_m, and the angle, θ_g, of the reference current for the grid inductor. Then using these two variables and phase of the grid voltage obtained by PLL, it build the reference current for the grid, $i_g{}^*$. Grid controller has a current loop with a PR controller with the resonant frequency of grid to make i_g track its reference. The P.R controller produce $i_t{}^*$which is the current drawn by just resonant circuit excluding the reactive power associated with HB capacitors and grid filter capacitor and inductor. Since the resonant controller input is power, this signal is multiplied by v_{Ci} and then it goes to the resonant controller.

B. Resonant Circuit Controller

The resonant controller receives an extra input d_2 in addition to p_t^*, v_{Ci} and v_{Co}. The output of it is $\underline{u}^T = [d_1\ \varphi_{12}\ d_3\ \varphi_{23}]$. For any set of input to it, it should find $\underline{u}^T$ which transfers p_t^*, minimize the RMS current through the resonant circuit and obtain ZVS for all the switching instances. Finding the analytical solution is very complex. Moreover, even if the answer is able to be found, it would be complicated and thus its implementation will be challenging. The answer can be found off-line using numerical methods. The input and output each are four-dimensional and each dimension of the input varies in a wide range. To implement the controller using offline calculation results, large amounts of memory is needed to save the four dimensional answers. Since the controller memories are very limited relying on off-line results, especially when high resolution control is needed, is not a solution for implementing the controller. Running the on-line numerical algorithm to solve the problem can be considered as a way of implementation. However, it can be challenging due to limited calculation time window available when using real-time control over converter.

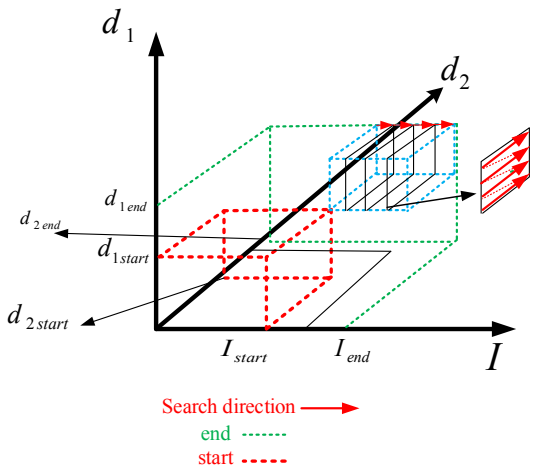

Fig. 4. Resonant circuit controller dyanmic search.

To solve some of these issues, online algorithm is used. It should find the optimal answer in a fixed calculation time independent of the input vector. This also allows for real-time optimal control of the converter.

The main resonant circuit controller, uses a real-time recursive algorithm to find the φ_{12}, φ_{23}, and d_3 that obtain ZVS at all switching instants and minimize the RMS current through the resonant circuit.

For every set of input, the trio of $(|\overline{I_{res}}|, d_1, d_3)$ is chosen to represent the operating point of the resonant converter. The area in which the optimal operating point exists needs to be searched. The controller with three-loops ought to be used to search the operating area in order to find the optimal operating point in

every calculation cycle. Fig.4 shows the operating area and search direction for every set of input or equivalently for every run of the algorithm or every calculation cycle. The flowchart that runs for every set of inputs is shown in Fig.5. It has three loops .$|\overline{I_{res}}|$-loop is the outset loop and it has an inner d_1-loop . d_1-loop has an inner d_3-loop.

For any set of inputs v_{Ci}, v_{Co}, $d_2$and $p_t{}^*$to this controller, it sweeps $|\overline{I_{res}}|$ incrementally starting from its minimum possible value and for every $|\overline{I_{res}}|$, it runs its internal d_1-loop. Inside this loop, it calculates $\angle\overline{I_{res}}$ from (9). Then from (12) and (13) it calculates $|\overline{V'_s}|$. Then, Inside this loop it runs d_3-loop. This loop is the most inner loop. Inside this loop it calculates φ_{23}, and evaluates ZVS conditions in (16)-(17). Finally if they are satisfied it returns the values of duty-cycles and phase-shifts to the PWM controller.

Choosing $|\overline{I_{res}}|$ as the variable for the outer loop is one of the actions taken to reduce the search time. Since conduction losses are proportional to $|\overline{I_{res}}|$ and algorithm sweep this value from its minimum possible value, the first operating point which satisfy the ZVS conditions is the operating point with minimum conduction loss and the algorithm can stop as soon as it finds an operating point. The algorithm then uses the information of the previous operating point to limit the next searching area and reduce the search time as well. For example, for the d_3-loop it uses d_{3old} by the gain of k_{d3} to initialize the loop as shown in (24).

$$d_{3\text{start}} = k_{d3} d_{3old} \tag{24}$$

Similarly, for the I-loop and d_1-loop the coefficients k_I and $k_{d1}$are used to initialize the loop using its old variables as is shown in (25) and (26).

$$I_{\text{start}} = k_{\text{I}} I_{old} \tag{25}$$

$$d_{1\text{start}} = k_{d1} \tag{26}$$

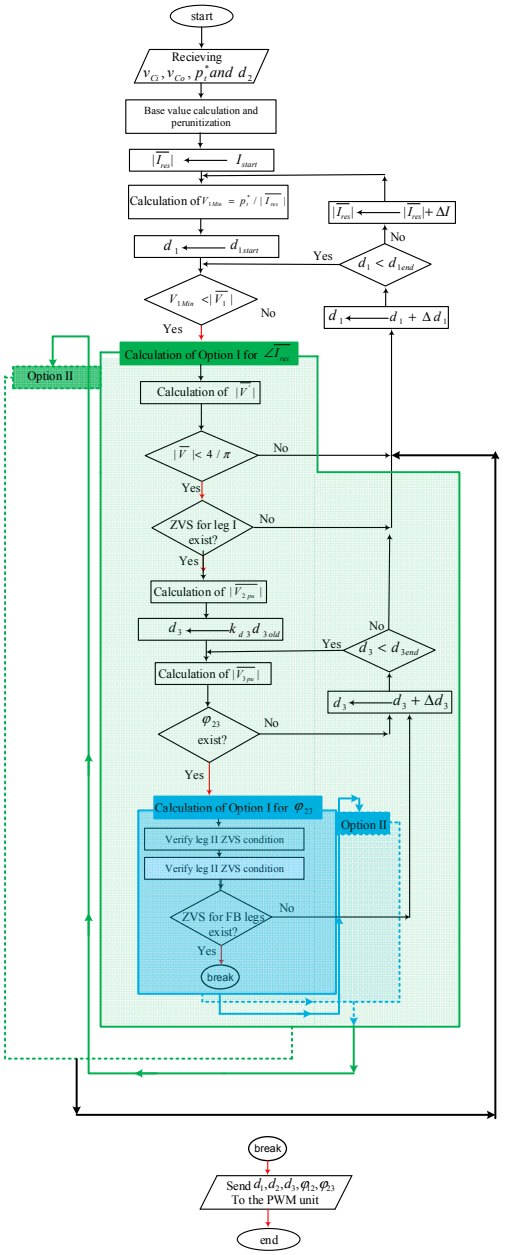

Fig. 5. Resonant circuit controller algorithm.

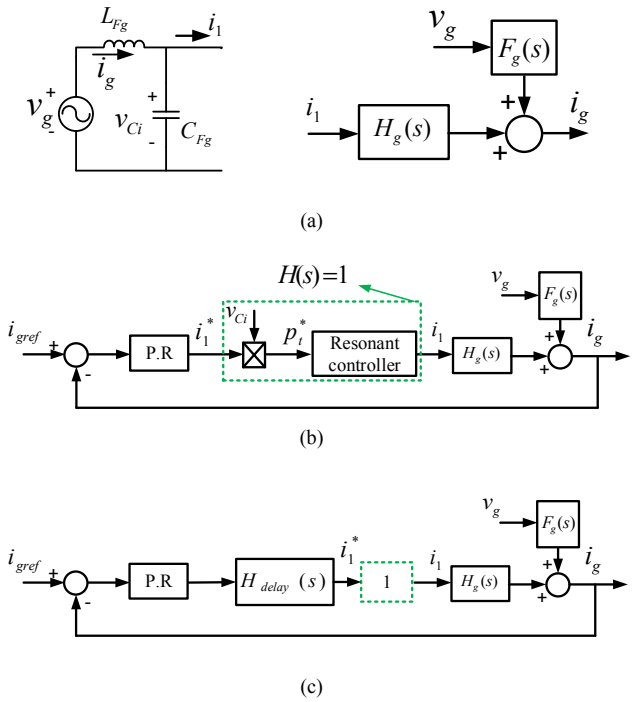

Fig. 6. Grid controlelr design: (a) input output model and (b) simplified model for controller design.

IV. DESIGN

The topology design can be broken down into grid filter, battery filter, decoupling circuit and resonant circuit design. The controller design can also be broken down into grid controller and decoupling controller design. The decoupling circuit and its controller design is similar to [13]. Grid filter and battery filter design is described in a qualitative way in [14]. Here more attention is paid on the design of grid controller and resonant tank.

A. Resonant tank Design

In order to obtain good performance in terms of efficiency for the wide range of operation including battery voltage, power and grid angle, the frequency or equivalently the reactance of the series branch in the resonant circuit varies for each operation point. Transformer turn ratio and optimal reactance for each operating point can be chosen so that the performance of the converter over the entire range of operation is optimum. After this stage, for a given optimal reactance and turn ratio, n, the resonant circuit parameters including L_{res}, C_{res1} and C_{res2} can be chosen to limit the operating frequency between the desired frequency limits, f_{max} and f_{min}. To do this, it is assumed that the total resonant capacitor transferred to the primary side is C_{res}. Assuming that the minimum and maximum values of the reactance found from the transformer and reactance design stage are X_{min} and X_{max} respectively. L_{res}, C_{res} can be found from (27) and (28) and consequently C_{res1} and C_{res2} can be found from (29) and (30).

$$L_{res} = \frac{1}{2\pi(f_{Min}^2 + f_{Max}^2)}(-f_{Min}X_{Min} + f_{Max}X_{Max}) \quad (27)$$

$$C_{res} = \frac{1}{2\pi}\left(\frac{1}{f_{Min}} + \frac{1}{f_{Max}}\right)\left(\frac{1}{f_{Max}X_{Min} + f_{Min}X_{Max}}\right) \quad (28)$$

$$C_{res1} = 2C_{res} \quad (29)$$

$$C_{res2} = 2C_{res}n \quad (30)$$

B. grid Cotroller Design

As was mentioned in the grid controller description, the ultimate output of the grid controller is $p_t{}^*$which goes to the resonant circuit controller. Resonant circuit controller, using its online algorithm, modulate $\underline{u}^T = [d_1\ \varphi_{12}\ d_3\ \varphi_{23}]$ so that $p_t{}^*$is transferred through the resonant circuit. In other words, the action of the resonant circuit controller together with the resonant circuit inject the average value of i_1 to grid filter from the resonant circuit side as shown in Fig.6(a).

Fig.6(b) shows the input-output model used for grid controller design. Transfer functions $H_g(s)$ and $F_g(s)$ are derived from Fig.6(a) and are shown in (31) and (32).

$$H_g(s) = \frac{1}{1 + L_gC_gs^2} \quad (31)$$

$$F_g(s) = \frac{C_gs}{1 + L_gC_gs^2} \quad (32)$$

To simplify the design, it is assumed that resonant circuit controller is perfect and draw the power $p_t{}^*$ from the grid filter. Therefore the current $i_t{}^*$ and i_t shown in Fig.6(b) are the same. The simplified model is shown in Fig.6(c). the delay $H_d(s)$ represent the calculation delay caused by DSP. Assuming that $i_g{}^*$is sinusoidal, the PR controller parameters can be tuned in such a way that the loop in Fig.6(c) is stable with zero steady state error at the grid frequency and has proper phase margin.

Here using classic pole-placement technique, P.R in Fig.6(c) is tuned. The transfer function of PR controller is shown in (33).

$$H_{PR}(s) = K_{pg} + \frac{K_r{\omega_r}^2 s}{{\omega_r}^2 + s^2} \quad (33)$$

For the converter with $L_{Fg} = 6.32\mu H$ and $C_{Fg} = 19\mu F$and grid frequency of $60Hz$ the following design is done using MATLAB pole-placement tool. The design criterion was to keep the poles all on the left hand side of the imaginary axis to keep the system stable and far enough from that to male the damping of those poles high. The parameters are $\omega_r = 120\pi$, $K_{pg} = 10^{-4}$ and $K_r = 60$.

TABLE I. SYSTEM PARAMETERS

component	resonant		decoupling		Battery filter		Grid filter		Switches		
	L_{res}	C_{res}	L_{dec}	C_{dec}	L_{Fb}	C_{Fb}	L_{Fg}	C_{Fg}	S_{FB}/S_{HB}	$S_{Decoupling}$	*transformer*
Proposed topology	$32.27\mu H/30A$ $/89.4gr$	$3.69\mu F$	$40\mu H/15A$ $/41.9gr$	$200\mu H$ 450v	$1\mu H$, $6A$	$100\mu F$ 450v	$6.32\mu H/7A/$ $8.6gr$	$19\mu F$ 400v	650V 60A $R_{ds}=50m\Omega$	-	$\mathbf{1:1/788gr}$
Topology in []	$20.32\mu H/40A$ $/139gr$	$4.46\mu F$	$40\mu H/15A$ $/41.9gr$	$200\mu H$ 450v	$1\mu H$ $/6A$	$100\mu F$ 450v	$11.66\mu H/7A$ $/10gr$	$11\mu F$ 400v	650V/60A $R_{ds}=50m\Omega$	650V/15A $\boldsymbol{R_{ds}=150m\Omega}$	$\mathbf{7:10/788gr}$

V. CALCULATION RESULTS

For the system with nominal values of $P_{m,n}=1kw$, $v_b=200-400V$, $v_g=230V$ and $f_s=90-400KHz$ the proposed converter is designed and the parameters are shown in table I. For this system a loss model considering switch conduction losses and magnetic losses including cupper and core loss is developed. Using this loss model, efficiency over the entire range of operation is calculated to evaluate the efficiency of the converter.

The optimal reactance, X_{opt}, for each operating point when $\theta_g=0$ and the equivalent optimal frequency, f_{opt} is shown in Fig.7. This figure shows how switching frequency should be modified for each operating point. The trend of frequency variation over the entire operating area when $\theta_g=\pi$ is similar to the Fig.7.

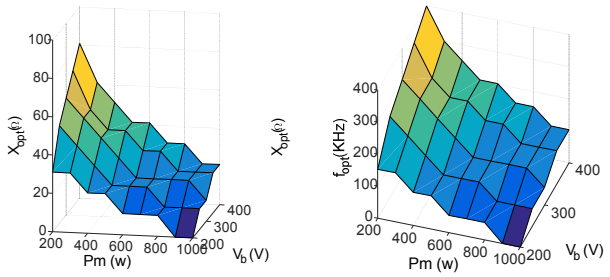

(a) (b)

Fig. 7. : Optimal rcatance (a) and optimal switching frequency (b) at $\theta_g=0$.

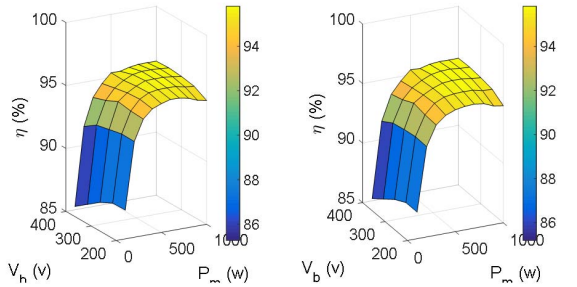

(a) (b)

Fig. 8. : Calculated efficiency for: (a) $\theta_g=0$ and (b) $\theta_g=\pi$.

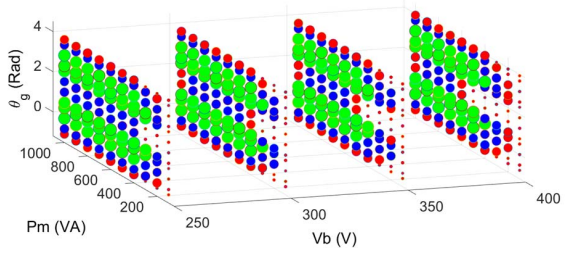

Fig. 9. efficiency within the entire operating area: (green: (η>95%), blue: (92% < η<95%) and red: (90% < η<92%).

The converter proposed in [12] has a similar topology with a separate decoupling circuit. It is designed for the same range of power, battery voltage, grid voltage and frequency and the results are shown in table I. Based on the loss model developed, the efficiency for this topology is calculated and is compared with the proposed topology. The results are shown in Fig.10. the best efficiency of both topologies is around 96% at the nominal operating point.

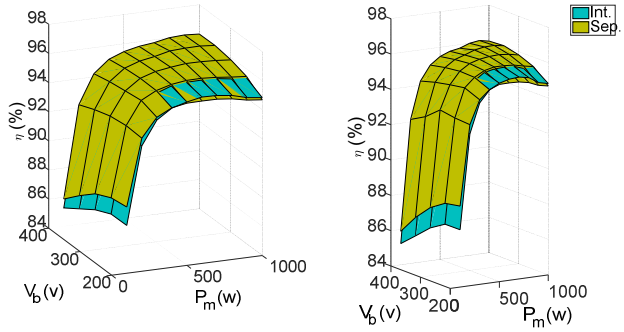

Fig. 10. : (a) optimal rcatance at $\theta_g=0$ and (b) optimal equvelent switching frequency at $\theta_g=\pi$.

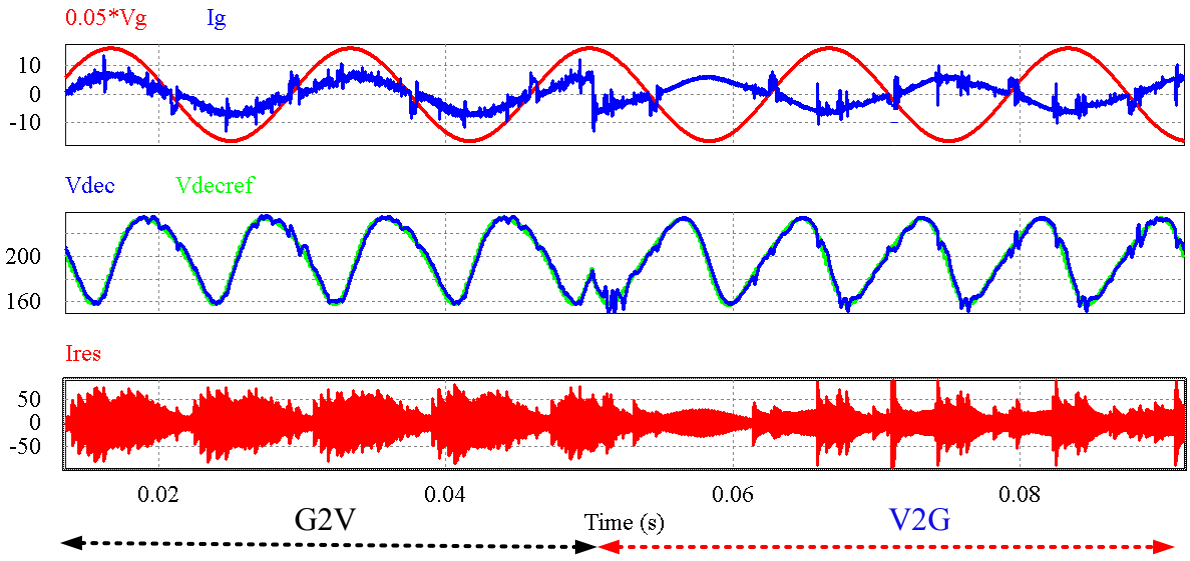

Fig. 11. Simulation results: G2V ($\boldsymbol{t < 0.05s}$) and V2G ($\boldsymbol{t > 0.05s}$).

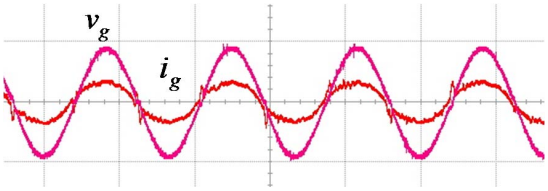

Fig. 12. Experimental results for G2V, $\boldsymbol{v_g}$(100V/div) and $\boldsymbol{i_g}$(5A/div) time scale (10ms/div).

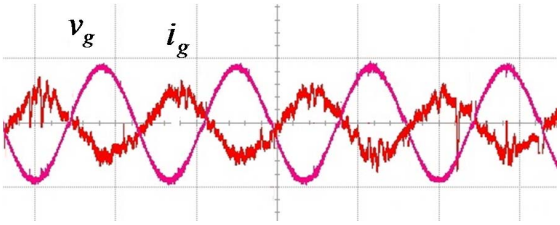

Fig. 13. Experimental results for V2G, $\boldsymbol{v_g}$(100V/div) and $\boldsymbol{i_g}$(1A/div) time scale (10ms/div).

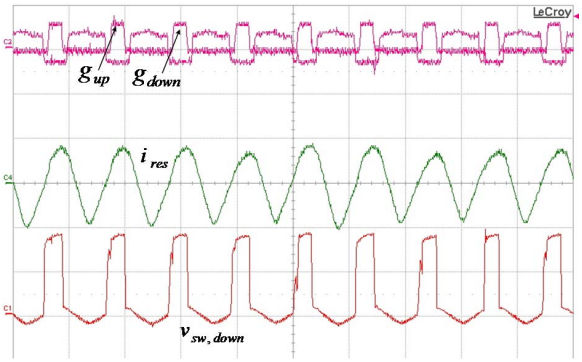

Fig. 14. Experimental results: ZVS operation of leg I, g_{up} and g_{down} (20V/div), i_{res} (10A/div), $v_{sw,down}$ (50V/div) and time scale (10μs/div).

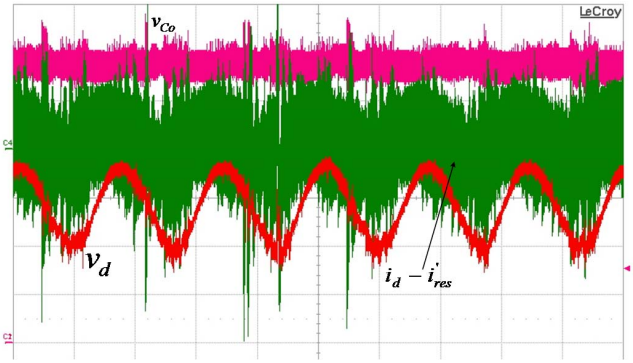

Fig. 15. Experimental results for decoupling circuit: v_d (20V/div), $i_d - i_{res}'$(10A/div), v_{Co}(20V/div) and time scale (5 ms/div).

VI. SIMULATION AND EXPERIMENTAL RESULTS

To verify the theory proposed, simulation results for the system with the parameters shown in Table II is carried out using PSIM software. Fig.11 shows the simulation results for different loading conditions. P_m is $1000w$, $V_b = 400v$ and $f_s = 80KHz$. Before t = 0.05s, the power angle, θ_g, is 0 and the converters act in G2V mode. The active filter is absorbing the 120Hz current ripple. At t = 0.05s the power angle changes into $\theta_g = \pi$ with the same peak power. Here the converter starts working in V2G mode.

TABLE II. SYSTEM SPECIFICATIONS

Parameter	value	Parameter	value
V_g	$230V$	C_{res}	$0.44\mu F$
V_b	$200-400V$	C_{HBp}	$12\mu F$
P_n	$1Kw$	C_{Fg}	$12\mu F$
f	$60-400$KHz	L_{Fg}	$22\mu H$
L_d	$40\mu H$	C_{Fb}	$100\mu F$
C_d	$190\mu F$	L_{Fb}	$1.1\mu H$
L_{res}	$42\mu H$		

Experimental results for the same system operating is presented in Fig.12 to Fig.15. Fig.12 shows the operation of the converter in G2V when θ_g=0 and $f_s = 90KHz$. As is seen the voltage and current are in phase. Fig.13 shows the operation of the converter for V2G when $\theta_g = \pi$ and $f_s = 100KHz$. The voltage and current are 180 degrees out of phase and power is returning to the grid from the battery. Fig.14 shows the ZVS operation of the leg I. The gating signals of the upper and lower active switches, g_{up} and g_{down}, after the gate driver circuit, is shown in this figure. The voltage across the drain-source of the lower switch of leg I is shown with $v_{sw,down}$. As it can be seen both for turn on and turn off of the lower switch happens with ZVS. Fig.15 shows the operation of the active filter or decoupling circuit. The current $i_d - i_{res}{}'$ is the current coming out of the midpoint of the leg pint. As is seen in this figure, the valley value and the peak value of this current is negative and positive respectively which determine ZVS operation of this leg.

VII. CONCLUSION

An electrolytic, capacitor-less, single-stage bi-directional AC-DC converter for EV charger with the appropriate four-part controller is presented. The current to the battery does not contain 120 Hz ripple, therefore lifetime of the battery is not degraded. E-Cap-less topology increases the reliability of the system, while the size and price is not increased. ZVS of all the switches enable the switching frequency to increase and make the converter more compact. Experimental and simulated results are presented.

REFERENCES

[1] M. Yilmaz and P.T. Krein, "Review of Battery Charger Topologies, Charging Power Levels, and Infrastructure for Plug-In Electric and Hybrid Vehicles," IEEE Transactions on Power Electronics, vol.28, no.5, pp.2151,2169, May 2013.

[2] M. Yilmaz and P. T. Krein, "Review of the Impact of Vehicle-to-Grid Technologies on Distribution Systems and Utility Interfaces," in IEEE Transactions on Power Electronics, vol. 28, no. 12, pp. 5673-5689, Dec. 2013.

[3] S. Norrga, "Experimental Study of a Soft-Switched Isolated Bidirectional AC–DC Converter Without Auxiliary Circuit," IEEE Transactions on Power Electronics, vol.21, no.6, pp.1580,1587, Nov. 2006.

[4] N.S. Vaishnav and H. Krishnaswami, "Single-stage isolated bi-directional converter topology using high frequency AC-link for charging and V2G applications of PHEV," Vehicle Power and Propulsion Conference (VPPC), 2011 IEEE , vol., no., pp.1,4, 6-9 Sept. 2011.

[5] G. Castelino, K. Basu, N. Weise and N. Mohan, "A bi-directional, isolated, single-stage, DAB-based AC-DC converter with open-loop power factor correction and other advanced features," IEEE International Conference on Industrial echnology (ICIT), 2012 , vol., no., pp.938,943, 19-21 March 2012.

[6] B. Koushki, A. Safaee, P. Jain and A. Bakhshai, "Review and comparison of bi-directional AC-DC converters with V2G capability for on-board EV and HEV," IEEE Transportation Electrification Conference and Expo (ITEC) 2014, vol., no., pp.1,6, 15-18 June 2014.

[7] M. Pahlevaninezhad, P. Das, J. Drobnik, P.K. Jain and A. Bakhshai, "A ZVS Interleaved Boost AC/DC Converter Used in Plug-in Electric Vehicles," IEEE Transactions on Power Electronics, vol.27, no.8, pp.3513-3529, Aug. 2012.

[8] H.L.Chan, "A new battery model for use with battery energy storage systems and electric vehicles power systems," Power Engineering Society Winter Meeting, 2000. IEEE, vol.1, no., pp.470,475 vol.1, 2000.

[9] C. J. Shin and J. Y. Lee, "An Electrolytic Capacitor-less Bi-Directional EV On-Board Charger Using Harmonic Modulation Technique," in IEEE Transactions on Power Electronics, vol. 29, no. 10, pp. 5195-5203, Oct. 2014.

[10] S. Li, J. Deng and C. C. Mi, "Single-Stage Resonant Battery Charger With Inherent Power Factor Correction for Electric Vehicles," in IEEE Transactions on Vehicular Technology, vol. 62, no. 9, pp. 4336-4344, Nov. 2013.

[11] M. Kwon, S. Jung and S. Choi, "A high efficiency bi-directional EV charger with seamless mode transfer for V2G and V2H application," 2015 IEEE Energy Conversion Congress and Exposition (ECCE), Montreal, QC, 2015, pp. 5394-5399.

[12] B. Kouski, P. Jain and A. Bakhshai, "Half-bridge full-bridge AC-DC resonant converter for bi-directional EV charger," 2017 IEEE Applied Power Electronics Conference and Exposition (APEC), Tampa, FL, 2017, pp. 3681-3687.

[13] B. Koushki, P. Jain and A. Bakhshai, "A bi-directional AC-DC converter for electric vehicle with no electrolytic capacitor," 2016 IEEE 7th International Symposium on Power Electronics for Distributed Generation Systems (PEDG), Vancouver, BC, 2016, pp. 1-8..

[14] B. Koushki, A. Safaee, P. Jain and A. Bakhshai, "A bi-directional single-stage isolated AC-DC converter for EV charging and V2G," 2015 IEEE Electrical Power and Energy Conference (EPEC), London, ON, 2015, pp. 36-44.